

# Cosmology in 2D: the concentration-mass relation for galaxy clusters

Carlo Giocoli<sup>1,2,3\*</sup>, Massimo Meneghetti<sup>2,3</sup>, Stefano Ettori<sup>2,3</sup>, Lauro Moscardini<sup>1,2,3</sup>

<sup>1</sup> *Dipartimento di Astronomia, Università di Bologna, via Ranzani 1, 40127, Bologna, Italy*

<sup>2</sup> *INAF - Osservatorio Astronomico di Bologna, via Ranzani 1, 40127, Bologna, Italy*

<sup>3</sup> *INFN - Sezione di Bologna, viale Berti Pichat 6/2, 40127, Bologna, Italy*

## ABSTRACT

The aim of this work is to perform a systematic study of the measures of the mass and concentration estimated by fitting the convergence profile of a large sample of mock galaxy cluster size lenses, created with the publicly available code MOKA. We found that the main contribution to the bias in mass and in concentration is due to the halo triaxiality and second to the presence of substructures within the host halo virial radius. We show that knowing the cluster elongation along the line of sight helps in correcting the mass bias, but still keeps a small negative bias for the concentration. If these mass and concentration biases will characterize the galaxy cluster sample of a wide field survey it will be difficult to well recover within one sigma the cosmological parameters that mainly influence the  $c - M$  relation, using as reference a 3D  $c - M$  relation measured in cosmological  $N$ -body simulation. In this work we propose how to correct the  $c - M$  relation for projection effects and for adiabatic contraction and suggest to use these as reference for real observed data. Correcting mass and concentration estimates, as we propose, gives a measurement of the cosmological parameter within  $1 - \sigma$  confidence contours.

**Key words:** galaxies: halos - cosmology: theory - dark matter - methods: analytical - gravitational lensing: strong

## 1 INTRODUCTION

Galaxy clusters represent a very important cosmic laboratory. Their abundance and structural properties are correlated with the content, the formation and the evolution history of the universe. Recent observational analyses have favored the dark energy as dominant component, contributing to the late accelerate expansion of the universe (Perlmutter et al. 1998, 1999), and the dark matter as the second one, made up of some kind of non-baryonic weakly interacting elementary particle, left over from the Big Bang, this represents the concordance  $\Lambda$ CDM model. Galaxy clusters, the most bound and late forming structures of the universe, possess a matter content which is compatible with the cosmic one (Ettori et al. 2009). About 85% of the total galaxy cluster mass is in form of dark matter, while 15% is attributed to baryons: 75% of which is in form of hot and 7% of cold gas, other baryon fractions count for the remaining 18%. For this reason, cluster number counts represent a very important probe for the nature of dark energy and matter, as like

as the study of their mass and concentration, that we will present and discuss in this work. Observing them at different wavelengths gives the possibility to study their whole content: the hot and cold gas, stars in galaxies and the presence of dark matter.

Numerical simulations of structure formation in the  $\Lambda$ CDM framework predict the halo concentration, defined as the ratio between the virial and the scale radii of the density profile, to be a monotonic function of the host halo mass: smaller haloes, forming at higher redshifts than larger ones, tend to possess a larger value of the concentration. Recently, increasing the force and the mass resolution in numerical simulation has given the possibility to span a very large halo mass range down to the size of dwarf-galaxies. Dolag et al. (2004); Neto et al. (2007); Macciò et al. (2007, 2008); Gao et al. (2008), interpreting the results of different numerical simulations, agree in finding a power-law relation between the average values of mass and concentration. On the other hand, more theoretical interpretations have been given to the average  $c - M$  relation by Zhao et al. (2009); Giocoli et al. (2012b), that relate the concentration to the time at which the main halo progenitor assembles a certain

\* E-mail: cgiocoli@oabo.inaf.it

fraction of their mass. Since observationally the halo formation time,  $t_f$  – defined as the time at which the main halo progenitor assembles half of its mass (Lacey & Cole 1993; Giocoli et al. 2007) – is not a direct measurable quantity, we need a good and unbiased estimate of the host halo mass and concentration to translate them in  $t_f$  (Giocoli et al. 2012b). The Cluster Lensing And Supernova survey with Hubble (CLASH) project (?), together with X-ray and ground-based optical observations, is providing the 2D mass distribution of a sample of 25 X-ray selected galaxy clusters. The clusters are selected as dynamically relaxed and span a range of redshifts going from  $z = 0.18$  up to  $z = 0.9$ . The cluster mass density distribution is reconstructed combining both strong and weak lensing analyses. The strong lensing analysis is performed thanks to the identification of multiple images (Zitrin et al. 2009) allowed by the excellent HST angular resolution. The reconstruction of the mass distribution is performed assuming that the galaxy cluster light traces the matter distribution made up of three components: the cluster galaxies, a dark matter halo and an external shear to account for additional ellipticity in the mass distribution. The weak lensing analysis, which probes the mass distribution outside the strong lensing region, is conducted using wider ground-based images obtained from Subaru (Umetsu et al. 2009; Okabe et al. 2010a), combined together with KPNO Mayall 4-m imaging and spectroscopy from MMT/Hctospec. In this case, selected background galaxies are identified from the wider cluster images and used to measure the observed shear and magnification. Deriving the mass profile simultaneously combining the strong and weak lensing analyses allows a very good determination of both the halo mass and concentration (Meneghetti et al. 2010b; Rasia et al. 2012). Unlike most other methods that are used to measure the mass and concentration of galaxy clusters, like X-ray analyses that need to assume hydrostatic equilibrium for the hot intracluster medium or satellite galaxy velocity distribution function that needs virial equilibrium (Becker et al. 2007), lensing analyses do not require any assumption of the dynamical state of the cluster. The interpretation based on the assumption of hydrostatic and virial equilibrium is sometimes complicated by the presence of massive and/or numerous substructures and by the fact that most clusters are not really relaxed.

Most of the analyses performed on combined weak and strong lensing observations tend to find clusters over-concentrated with respect to what is expected in a  $\Lambda$ CDM universe. This bias can be due both to intrinsic projection effects – main halo triaxiality (Meneghetti et al. 2007b) and/or presence of substructures along the line of sight – and to the presence of a massive background structure (Coe et al. 2012). To be able to recover a good and unbiased estimate of the dark mass and concentration is important to better constrain cosmological parameters.

Meneghetti et al. (2010b); Rasia et al. (2012), studying galaxy clusters extracted from numerical simulations, have shown that fitting projected quantities, using a Navarro et al. (1997) (hereafter; NFW) function, recovers a mass that could be underestimated down to 10 – 15%. The halo mass tends to be more biased generally when the 2D projected mass is unrelaxed due to presence of nearby structures.

Recently, Bahé et al. (2012) have produced mock observations of a sample of massive clusters extracted at red-

shift  $z = 0.2$  from the Millennium Simulation (Springel et al. 2005), to obtain a projected estimate for both halo mass and concentration through simulated weak lensing only analysis. They showed that the slope and the normalization of the derived 2D  $c-M$  relation tend to be lower than the underlying 3D ones by 40 and 15 percent respectively. An underestimation of the mass measured from weak gravitational lensing has been also found by Becker & Kravtsov (2011), using cluster-size haloes extracted from a numerical simulation. Their analysis includes correlated and uncorrelated LSS plus gaussian noise in the tangential shear measurement.

Light travelling from background sources to the observer is also deflected by the presence of large scale structures (LSS) along the line of sight: the observed lensing signal is a combination of the cluster and the cosmic shear signal (Hoekstra 2003). This combination limits the accuracy with which both mass and concentration can be estimated, not introducing any particular bias. Hoekstra et al. (2011), also using the Millennium Simulation results, derived that this contribution adds an error budget which is comparable to the statistical errors. In order to bypass the effect of LSS and also the errors and the biases that could be introduced on the cluster mass reconstructions by the data analysis software pipelines, we build a large sample of galaxy cluster convergence maps using the publicly available software MOKA (Giocoli et al. 2012a), and fit their derived spherical averaged profile to recover their mass and concentration.

Through this work we use a  $\Lambda$ CDM reference model, according to WMAP7-year results (Komatsu et al. 2011):  $\Omega_m = 0.272$  (DM+baryons),  $\Omega_\Lambda = 0.728$ ,  $w = -1$ ,  $\sigma_8 = 0.809$  and  $h = 0.704$  at  $z = 0$ .

The paper is organized as follow. In Section 2 we summarize the ingredients used to create our cluster size-haloes. In Section 3 we quantify the bias and scatter caused by intrinsic halo properties. Section 4 is devoted to study how well cosmological parameters can be constrained using the  $c-M$  relation of objects extracted from a wide field survey. Summary and conclusions are discussed in Section 5.

## 2 THE METHOD

### 2.1 The MOKA Code

MOKA (Giocoli et al. 2012a) is a new and fast code able to create realistic gravitational lenses, whose size spans from galaxies up to clusters of galaxies<sup>1</sup>. The algorithm uses the recent results obtained from numerical simulations to model the structural properties of the lenses. In creating cluster 2D-maps MOKA is very fast, its utilization is friendly allowing the possibility of switching on and off different halo properties. The user can also easily change and redefine the characteristics of the main halo, of subhaloes and of the bright central galaxy.

### 2.2 Presence of Substructures and of a Bright Central Galaxy

In this work we produced a set of simulations creating a sample of different galaxy cluster size lenses at various red-

<sup>1</sup> web page: [cgiocoli.wordpress.com/research-interests/moka](http://cgiocoli.wordpress.com/research-interests/moka)

shifts. We have divided the haloes in nine mass bins from  $10^{13.5}$  up to  $10^{15.5}M_{\odot}/h$ , logarithmically equally spaced with  $d \log(M) = 0.25$ . In each mass bin, with mass  $M_{vir}$ , we have generated a sample of 128 lenses, that differ in concentration  $c_{vir}$ , randomly sampling a log-normal distribution, around the average value for that mass, with a given  $\sigma_{\ln c}$ , and in subhalo abundance. In what follows we summarize the ingredients included in the input file of the algorithm.

- One of the main result obtained studying virialized structures in numerical simulations is that haloes possess a relatively flat density profile  $\propto r^{-1}$  near the center and steeper  $\propto r^{-3}$  outside (Navarro et al. 1997). The scale radius  $r_s$  where the slope changes defines the halo concentration  $c_{vir} \equiv R_{vir}/r_s$ . For each halo, the smooth halo component is modelled with a NFW profile, to which is assigned a concentration  $c_{sm}$  such that:

$$\rho_{NFW,vir}(r|M_{vir},c_{vir}) = \rho_{NFW,s}(r|M_{sm},c_{sm}) + \sum_{i=1}^{N_{tot}} \rho_{sub}(r-r_i|m_{sub,i}), \quad (1)$$

where the subscript *vir*, *sm* and *sub* refer to the total halo, the smooth component and the substructures respectively,  $r_i$  indicates the distance of the subhalo from the host halo center and  $\rho_{sub}(< r)$  is the subhalo density profile. The equation above is solved numerically by minimizing:

$$\chi^2(c_{sm}) = \left\{ \rho_{NFW,vir}(r|M_{vir},c_{vir}) - \left[ \rho_{NFW,s}(r|M_{sm},c_{sm}) + \sum_{i=1}^{N_{tot}} \rho_{sub}(r-r_i|m_{sub,i}) \right] \right\}^2. \quad (2)$$

- In the standard scenario of structure formation haloes collapse as consequence of gravitational instability, with the small systems assembling first, in a denser universe, than the large ones (Wechsler et al. 2002). This translates in small haloes to be typically more concentrated than the large ones. In our model we use the Zhao et al. (2009) relation to take into account this effect, which relates the concentration of the halo with the time  $t_{0.04}$  at which the main halo progenitor assembles 4% of its mass through the equation:

$$c_{vir}(M_{vir},z) = 4 \left\{ 1 + \left[ \frac{t(z)}{3.75t_{0.04}} \right]^{8.4} \right\}^{1/8}. \quad (3)$$

According to this model we estimate the scatter in concentration at fixed halo mass using the scatter in  $t_{0.04}$  from the generalized formation redshift distribution derived by Giocoli et al. (2012b). In Figure 1 we show the redshift evolution of the scatter in concentration as a function of redshift. From the figure, we notice that at low redshift the scatter is consistent with the results of numerical simulations (Jing 2000; Jing & Suto 2002; Wechsler et al. 2002; Dolag et al. 2004; Sheth & Tormen 2004; Neto et al. 2007) to be of the order of 0.23, while at high redshift  $\sigma_{\ln c}$  drops down due to the contraction of the typical halo merging time scale. However, the decrease of the scatter at high redshift does not seem to exist in numerical simulation, as recently noticed by Bhattacharya et al. (2011). The difference can be due to the fact that numerical simulations are limited in mass resolution going to higher  $z$  or that the scatter in  $c_{vir}$  at a fixed mass is not totally due to the different assembly halo histories.

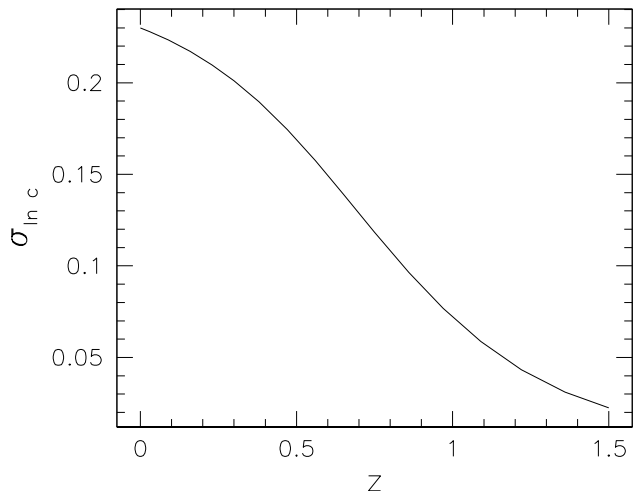


**Figure 1.** Scatter in concentration  $\sigma_{\ln c}$  at a fixed host halo mass as a function of  $z$  due to the scatter in time when the main halo progenitor assembles 4% of its mass. The scatter has been obtained mass averaging the scatter at fixed halo mass of a sample of haloes with mass larger than  $3.16 \times 10^{13}M_{\odot}/h$ .

- The improvement of the computational resources has given the possibility to increase mass and force resolution in numerical simulations. One of the first results revealed by this improvement is that haloes are not completely smooth but made up of different clumps. Since merging events are not totally efficient, these clumps represent the core of progenitor haloes accreted during the growth of the main halo progenitor (Springel et al. 2001b; Gao et al. 2004; Giocoli et al. 2008). Different studies based on the analysis of numerical simulations have converged on the fact that the subhalo mass function has a power-law distribution with a slope  $\alpha = -1.9$ . In modeling the subhalo population in MOKA we will use the model proposed by Giocoli et al. (2010a) which takes into account the dependence on redshift and on the host halo mass of the distribution, plus the scatter at fixed mass due to the different assembly history; this means that the scatters of the concentration and subhalo mass function, for a fixed halo mass, are not independent but are correlated: haloes more concentrated, and so forming at higher redshift, are more relaxed and typically tend to possess less substructures (Gao et al. 2004; Giocoli et al. 2008). We will populate the host halo sampling the subhalo mass function down to a mass resolution of  $10^{10}M_{\odot}/h$ , which is of the order of the minimum subhalo mass resolved in current cosmological numerical simulations (Springel et al. 2005; Gottloeber et al. 2006; Boylan-Kolchin et al. 2009).

- The subhalo density distribution inside the hosts tends to follow that of the host dark matter component. However, the combined effect of gravitational heating and tidal stripping does not allow subhaloes to be present in the central region of the cluster, mainly dominated by the density profile of the smooth component that increases like  $r^{-1}$ . This translates into a clump density distribution which is less concentrated and shallower than the NFW profile toward the centre. To spatially locate the subhaloes within the virial radius of the cluster we will adopt the relation by Gao et al. (2004), since it takes into account these effects being extracted from simulated clusters.

- Haloes trace the dark matter density field in the Universe and their clustering is a function of both the mass and the redshift. Their mutual gravitational interaction tends to pull and stretch their matter distribution making the haloes triaxial. We model the halo triaxiality using the results by Jing & Suto (2002) from numerical studies. This model correlates the axial ratios  $e_a/e_c$  and  $e_b/e_c$  ( $e_a < e_b < e_c$ ) with the typical collapsed mass  $M^*$ , at the considered redshift, and the matter content of the universe  $\Omega_m$ ; apart from this no other tighter correlation between the halo triaxiality and its formation time is assumed.

- Orbiting in the potential well of the host, subhalo density profile tends to be modified since (i) the particles are heated at the local temperature of the host, (ii) pushed toward the tidal radius and (iii) eventually stripped. This phenomenology modifies the initial NFW profile into something that is well described by a singular isothermal sphere (SIS) (Metcalf & Madau 2001). The radius of the subhaloes is computed in such a way to preserve the subhalo mass  $m_{sub}$  and is defined as:

$$R_{sub} = \frac{Gm_{sub}}{2\sigma_v^2}. \quad (4)$$

As discussed in Giocoli et al. (2012a) we notice that typically, if the subhalo is located at a distance  $r$  from the host halo center, the following condition is valid  $R_t(r) \leq R_{sub}$ , with  $R_t(r)$  defined as (Tormen et al. 1998):

$$R_t = r \left\{ \frac{m_{sub}}{[2 - \partial \ln M_{vir}(r) / \partial \ln r] M_{vir}(r)} \right\}^{1/3}, \quad (5)$$

where  $M_{vir}(r)$  represents the mass density profile of the host halo. The SIS profile will be used to model the matter density distribution around clumps.

- In the standard scenario (White & Rees 1978), the structure formation process is driven by the dark matter component. Baryons, feeling the halo gravitational potential, shock, cool and eventually form stars. This phenomenology drives the formation of a massive and bright galaxy at the center of the main halo progenitor. The correct modeling of the bright central galaxy (BCG) is important since it influences the lensing cross section of galaxy clusters (Meneghetti et al. 2003). The central galaxy population is modeled in MOKA using the halo occupation distribution (HOD) approach. We use the relation by Wang et al. (2006) to estimate the BCG stellar mass  $M_{BCG}$ , assuming that  $M_{BCG}$  correlates with the depth of the potential well of the halo within which it formed, thus:

$$M_{BCG} = \frac{2M_{star,0}}{(M_{vir}/M_\odot)^{-\alpha} + (M_{vir}/M_\odot)^{-\beta}}. \quad (6)$$

In this relation, we include a Gaussian scatter in  $M_{BCG}$  for given host halo mass with  $\sigma_{M_{BCG}} = 0.148$ , we set the parameters  $\alpha = 0.39$ ,  $\beta = 1.96$ ,  $\log(M_{star,0}) = 10.35$  and  $M_0 = 3.16 \times 10^{11} M_\odot/h$  (see Wang et al. (2006) for more details about the parameters).

- The BCG stellar density profile is described following the Hernquist (1990) profile:

$$\rho_{star}(r) = \frac{\rho_g}{(r/r_f)(1+r/r_g)^3}, \quad (7)$$

where the scale radius  $r_g$  is related to the half-mass (or effective) radius  $R_e$  by  $r_g = 0.551R_e$ . As done by Keeton (2001) we define the effective radius to be  $R_e = 0.003R_{vir}$ . The

scale density  $\rho_g$  can be estimated by the definition of the total mass of a Hernquist model:

$$\rho_g = \frac{M_{star}}{2\pi r_g^3}. \quad (8)$$

We checked the robustness of our results using a Jaffe (1983) profile which keeps unchanged our results.

In Table 1 we summarize the whole set of simulations we have performed: the first two samples, SPH and SPHwBCG, assume the haloes to be spherical, while the last two, ELLwBCG and ELLwBCGwADC, consider the haloes to be triaxial. In the latter case the axial ratios are obtained randomly sampling the distributions suggested by Jing & Suto (2002). We also notice that the last three samples include the presence of a BCG. In all samples we included the contribution from the subhalo population. We recall the reader that the total halo mass  $M_{vir}$  is defined as the sum of all components, so:

$$M_{vir} = M_{smooth} + \sum_{i=1}^{N_{tot}} m_{sub,i} [+M_{BCG}]. \quad (9)$$

In SPHwBCG and ELLwBCG, the presence of a dissipative baryonic component in the host halo centre does not influence the dark matter density distribution. This phenomenology, acting on the dark matter component mainly in proximity of the host halo centre and known as adiabatic contraction (Blumenthal et al. 1986; Rix et al. 1997; Keeton 2001; Gnedin et al. 2011). The effects of baryons on the total mass profile are generally found to only modify halo concentrations at the 10% level, although some studies suggest that low mass systems may be significantly affected by baryonic cooling (Fedeli 2011). ELLwBCGwADC includes adiabatic contraction, and in Appendix A we discuss how the mass and concentration estimates are biased with respect to the ELLwBCG sample.

As example, in the Figure 2 we show the spherical averaged convergence profiles and the maps of two clusters, with substructures and BCG. In the top panels, we present the case of a spherical system while in the bottom panels we show a triaxial one (the label reports the values of the axial ratios projected in the plane of the lens and along the line of sight). We underline that in all our simulations we do not consider perturbations of the projected matter density due to the large scale structures along the line of sight (Hoekstra 2003). This is because we are mainly interested to understand how the halo properties themselves affect the recovered mass and concentration fitting a projected quantity. The map of each halo is resolved with a resolution of  $1024 \times 1024$  pixels up to the virial radius  $R_{vir}$  defined as the radius enclosing the density contrast predicted by the spherical collapse model (Eke et al. 1996). The profile is built binning linearly the convergence on annulus of 8 pixels on which also the rms is estimated, showed by the shaded region in the convergence profile of the figure.

### 3 FITTING THE CONVERGENCE PROFILE

The estimate of the total galaxy cluster mass is important because it is by far the most accurate predicted halo property from theory. Ongoing and future surveys require an estimate of the mass with a bias smaller than 10% in order to

**Table 1.** List of Simulation sets performed with MOKA 1.5

Simulation set name	Smooth component	Substructures	BCG	Adiabatic Contraction
SPH	spherical	yes	no	no
SPHwBCG	spherical	yes	yes	no
ELLwBCG	triaxial	yes	yes	no
ELLwBCGwADC	triaxial	yes	yes	yes

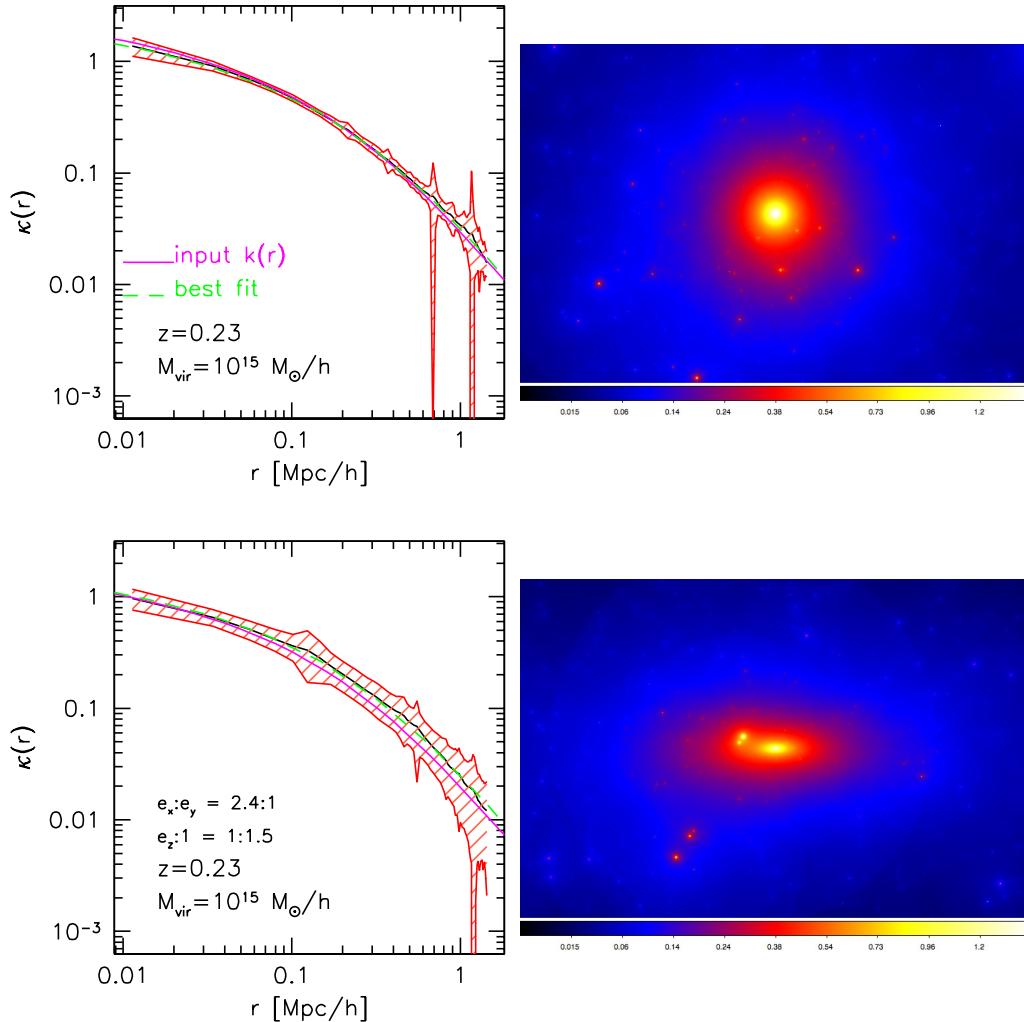


**Figure 2.** *Top panels:* spherical averaged convergence profile of a spherical halo with substructures and BCG created with MOKA. The shaded region shows the rms of the average convergence in each annulus 8 pixels large. The right subpanel shows the convergence map of the central region. *Bottom panels:* spherical averaged convergence profile of a triaxial halo with substructures and BCG. In the label we show the values of the components of the axial ratios in the plane of the lens and along the line of sight. The solid and dashed line show the input and the best fit converge profile respectively. The right subpanel shows the convergence map up to half virial radius of the triaxial halo.

allow the usage of cluster counts as cosmological probe. However, Okabe et al. (2010b); Oguri et al. (2012) showed that the combination of mass and concentration estimates, from weak and weak+strong lensing measurements respectively, can be used as an additional cosmological probe through the  $c - M$  relation. These results have revealed a good agreement with the theoretical predictions for massive clusters but a steeper dependence of the concentration on the mass with what pure  $N$ -body simulations predict. As discussed

by Fedeli (2011) (see also Appendix A), the steepening of the  $c - M$  relation reflects the response of the dark matter density distribution to the presence of the cold baryons in the central regions of haloes, that is stronger in less massive, then in more massive haloes, since baryon cooling and star formation are more efficient in those systems (Conroy et al. 2007a; Andreon 2010). In this direction it is very important to understand the scatter and the bias in the mass and in the concentration estimated when fitting a projected

quantity: the convergence profile. We are aware of the fact that the convergence is not a direct observable and that the most standard way to measure the cluster mass profile with weak lensing is the tangential shear, but our work is meant to study the scatter and the bias introduced in the mass and in the concentration measurements going from a 3D to a 2D quantity of the measurement halo profiles. Since our idea is to illustrate the intrinsic scatter and the bias in the mass and concentration estimates, obtained when fitting projected quantities, we present and discuss our results assuming no observational error in the cluster converge map. The situation would have been different if we had used the tangential shear profile, where the dominant source of noise is the intrinsic ellipticity distribution of background galaxies  $\sigma_e \approx 0.3$  (Okabe et al. 2010a) that gives a Gaussian noise in each region of area  $A$  where is measured given by:

$$\sigma_s^2 = \frac{\sigma_e^2}{n_{gal}A}, \quad (10)$$

where  $n_{gal}$  represents the background galaxy density distribution, that goes from 10 gal/arcmin<sup>2</sup> for Dark Energy Survey (DES) or similar to 40 gal/arcmin<sup>2</sup> for deep ground based observations like Large Synoptic Survey Telescope (LSST) or space based observation like Euclid. It is worth mentioning that for high quality observations with large source densities, the effect of shape noise becomes comparable or subdominant with respect to the intrinsic source scatters: triaxiality, correlated (haloes and subhaloes around 3 *Mpc/h* from the cluster) and uncorrelated large-scale structures (systems more distant than 3 *Mpc/h* from the cluster). To isolate the effects of halo substructures and triaxiality we will describe our results using the cluster convergence profile. We also underline that the results are specific to the method chosen for measuring the halo properties (the converge profile). In order to compare the rms of the convergence with the statistical observational noise, we show in Figure 3 the convergence profile of three clusters located at redshift  $z = 0.03, 0.23$  and  $0.47$ . In each panel the shaded region represents  $\sigma_\kappa$  while the solid curves enclose the statistical observational noise  $\sigma_s$ . We have considered 35, 30 and 25 gal/arcmin<sup>2</sup> for the cluster located at  $z = 0.03, 0.23$  and  $0.47$ , respectively. From the figure we notice that while in the inner region of the clusters the two errors are almost identical, going toward the virial radius the noise expected from the intrinsic ellipticities of source galaxies becomes larger than the rms of the convergence.

For each halo the spherical averaged convergence profile is best fitted using a single component NFW function in order to obtain a simultaneous estimate for both the mass  $M_{fit}$  and the concentration  $c_{fit}$ . These are obtained considering that, if we define  $x$  and  $y$  as the coordinates on the lens plane, the convergence  $\kappa(r)$  of a NFW profile can be written as (Bartelmann 1996; Meneghetti et al. 2003):

$$\Sigma_{NFW}(x, y) = \frac{2\rho_s r_s}{r^2 - 1} F(r), \quad (11)$$

where  $r \equiv \sqrt{x^2 + y^2}/r_s$ , and  $F(r)$ :

$$F(r) = \begin{cases} 1 - \frac{2}{\sqrt{r^2 - 1}} \arctan \sqrt{\frac{r-1}{r+1}} & r > 1, \\ 1 - \frac{2}{\sqrt{1-r^2}} \operatorname{arctanh} \sqrt{\frac{r-1}{r+1}} & r < 1, \\ 0 & r = 1; \end{cases}$$

$r_s$  is the scale radius, defining the concentration  $c_{vir} \equiv R_{vir}/r_s$ , and  $\rho_s$  is the dark matter density at the scale radius,

$$\rho_s = \frac{M_{vir}}{4\pi r_s^3} \left[ \ln(1 + c_{vir}) - \frac{c_{vir}}{1 + c_{vir}} \right]^{-1}, \quad (12)$$

and so

$$\kappa_{NFW}(r) = \frac{\Sigma_{NFW}(r)}{\Sigma_{crit}}, \quad (13)$$

where  $\Sigma_{crit} = c^2 D_s / (4\pi G D_l D_{ls})$  is the critical surface mass density, depending on the angular-diameter distances  $D_l$ ,  $D_s$  and  $D_{ls}$  from the observer to the lens, to the source, and from the lens to the source, respectively. From the equations above, since  $\kappa_{NFW}(r)$  depends both on halo mass and concentration,  $M_{fit}$  and  $c_{fit}$  are obtained by minimizing the  $\chi^2$  function:

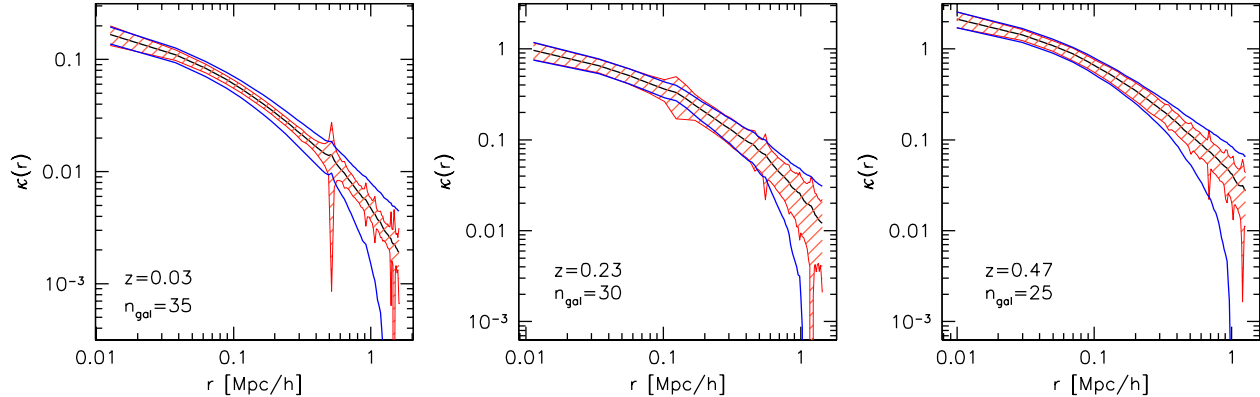
$$\chi^2(M_{fit}, c_{fit}) = \sum_{i=1}^{N_{radial\ bins}} \frac{[\kappa_{NFW}(r_i | M_{fit}, c_{fit}) - \kappa(r_i)]^2}{\sigma_{\kappa,i}^2}, \quad (14)$$

where  $N_{radial\ bins}$  represents the number of radial bins on which the convergence profile is estimated. In the default setting wich considers the whole profile  $[0, 1]R_{vir}$  the number of radial bins is 64, since the map is made by  $1024 \times 1024$  pixels and the profile is linearly built on annuli of 8 pixels.

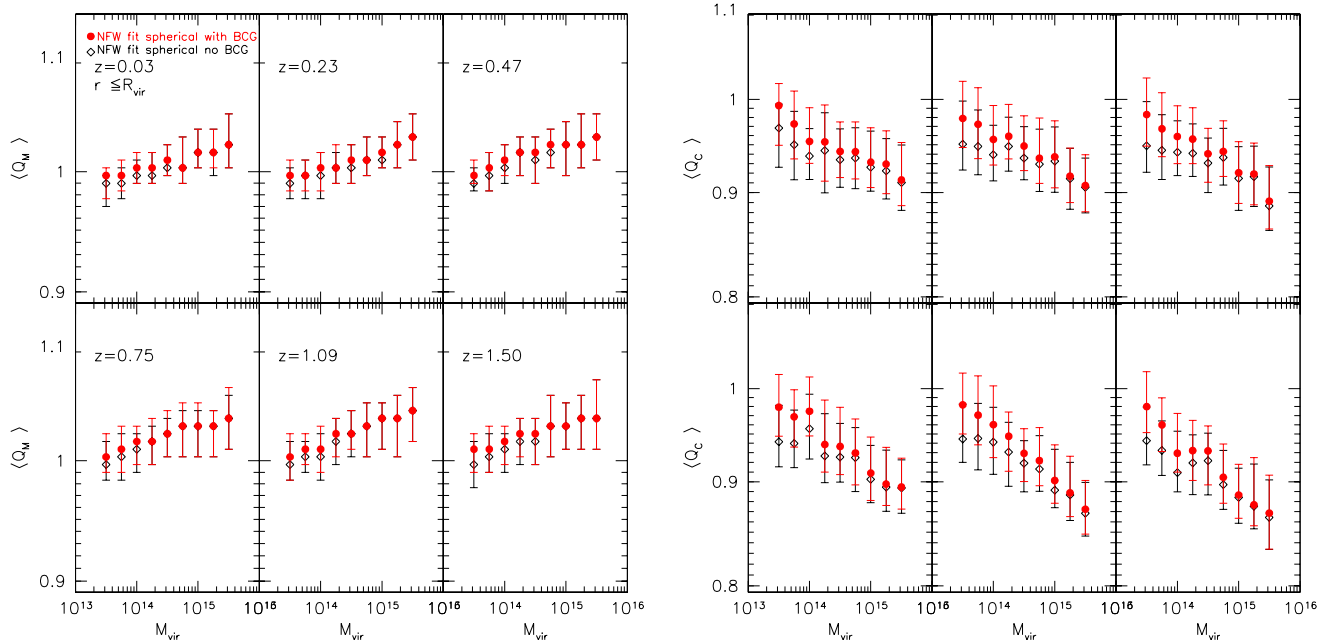
### 3.1 Spherical Haloes

Figure 4 shows the rescaled mass  $Q_M \equiv M_{fit}/M_{vir}$  and concentration  $Q_C \equiv c_{fit}/c_{vir}$  estimates – where  $M_{vir}$  and  $c_{vir}$  represent the true halo mass and concentration – as a function of  $M_{vir}$  for the samples SPH (open diamonds) and SPHwBCG (filled circles) at six different redshifts. The estimates have been obtained by fitting the profile up to the halo virial radius: this in practice would mean that for a realistic cluster we would need to combine both strong and weak lensing data. The different data points with error bars represent the median and the two quartiles, respectively of the distribution in each mass bin. From the left figure we notice that the halo mass is very well recovered without any bias and with an error of only few percents. The small trend with the halo mass is due to the presence of substructures that contaminate the projected mass distribution: the most massive haloes possess a larger fraction of mass in substructures, because of their later formation time, with respect to the least massive systems (Gao et al. 2004; De Lucia et al. 2004; van den Bosch et al. 2005). Unlike the mass, the estimated concentration (right panels) shows a negative bias and a decreasing behavior with the host halo mass, and so with the subhalo abundance. From this figure we notice that the concentration estimate is more influenced by the presence of substructures in the 2D map than the mass estimate. At the smallest masses, the BCG seems to play a more relevant role, adding an additional bias of few percent.

To discuss the importance of the radial range used when fitting the convergence profile, in Figure 5 we again show the estimated mass and the concentration as a function of the true halo mass, for the same two halo samples discussed before. In this case we show how the estimated masses and concentrations depend on the radial range on which the fit is performed. In the upper panels, we fit the profile between



**Figure 3.** Convergence profile of three galaxy cluster-size haloes with  $M_{vir} = 10^{15} M_{\odot}/h$ , located at three different redshifts. In each panel, the shaded region represents the rms  $\sigma_{\kappa}$  of the average convergence measured in each annulus, while the solid curves represent the noise expected from the intrinsic ellipticities of source galaxies  $\sigma_s$ .



**Figure 4.** Median rescaled mass (left panels) and concentration (right panels) estimates as a function of the halo mass, for spherical substructured haloes at six different redshifts. The mass of each halo has been estimated by best fitting the spherical averaged convergence profile of each halo up to the virial radius  $R_{vir}$ , with a NFW function varying both the mass and the concentration. The two different data points refer to haloes without (open diamonds) and with (filled circles) the bright central galaxy. The error bars enclose the first and the third quartiles.

$[R_{min}, R_{max}]/R_{vir} = [0, 1], [0, 0.5], [0, 0.1]$  (upper panels of Fig. 5),  $[0.1, 1], [0.25, 1]$  and  $[0.5, 1]$  (lower panels). Results are shown only for haloes at redshift  $z = 0.23$ , since we verified that they do not depend on redshift. It is worth noticing that we do not observe significant differences apart from the following cases: (i) in the fit over the radial range  $[0.25, 1]R_{vir}$ , where the scatter is almost double; (ii) when the region  $[0, 0.1]R_{vir}$  is considered: it roughly corresponds to the strong lensing region where the contribution from the BCG is comparable to that of the dark matter component, while in presence of a BCG the mass is slightly underestimated almost the opposite is valid for the concentration (see the different data points); (iii) in the fit over the radial

range  $[0.5, 1]R_{vir}$ , where both mass and concentration are overestimated by a factor of 1.5 and 3.5, respectively.

In order to quantify how much the presence of substructures in host haloes biases the mass and the concentration estimates, we have divided our sample in haloes with more and less substructures. In each mass bin we estimate the median host halo mass fraction in substructures  $\langle f_{sub} \rangle$  and we define a halo as “substructured” if its  $f_{sub}$  is larger than the median,  $f_{sub} > \langle f_{sub} \rangle$ . On the contrary, “unsubstructured” haloes have  $f_{sub} < \langle f_{sub} \rangle$ . In Figure 6 we show the estimated mass and concentration at different redshifts (as in Figure 4) for the samples of substructured (open triangles) and unsubstructured haloes (filled circles). The haloes are

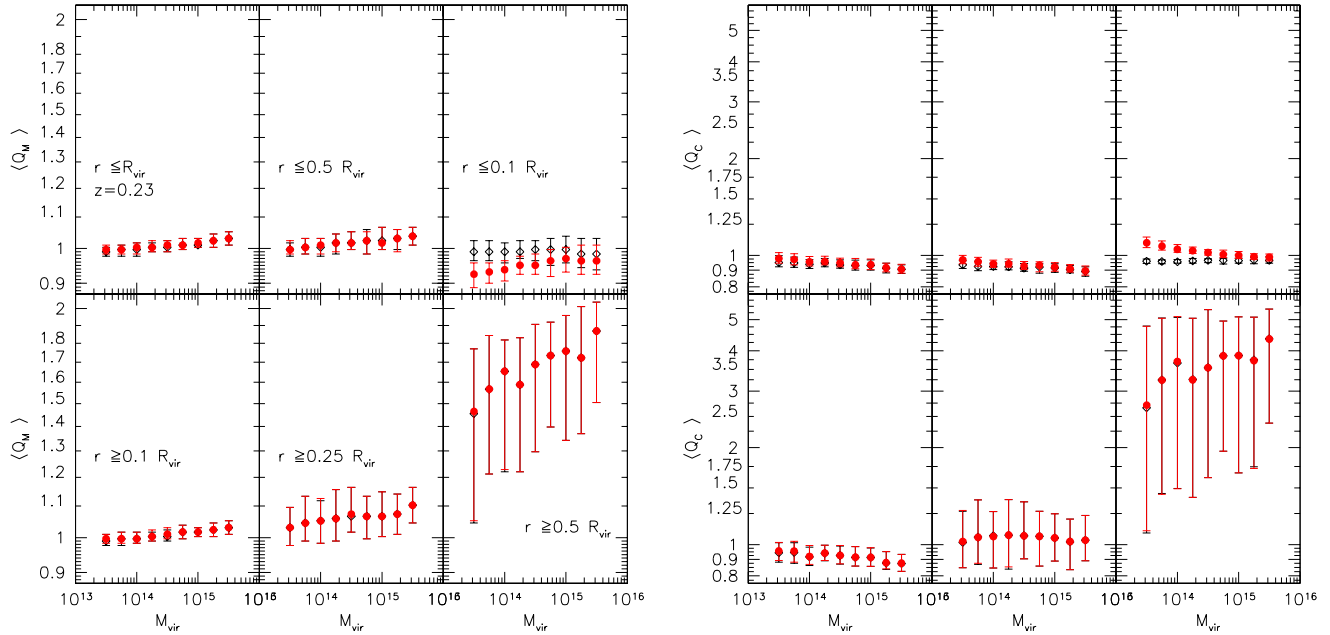


**Figure 5.** Median rescaled mass (*left panels*) and concentration (*right panels*) estimates as a function of the halo mass, for spherical and substructured haloes at redshift  $z = 0.23$ . The top panels show the relation obtained fitting the spherical averaged convergence profile up to  $R_{vir}$ ,  $0.5R_{vir}$  and  $0.1R_{vir}$ ; while the bottom ones from  $R_{vir}$  down to  $0.1R_{vir}$ ,  $0.25R_{vir}$  and  $0.5R_{vir}$ . Symbols and error bars are as in Figure 4.

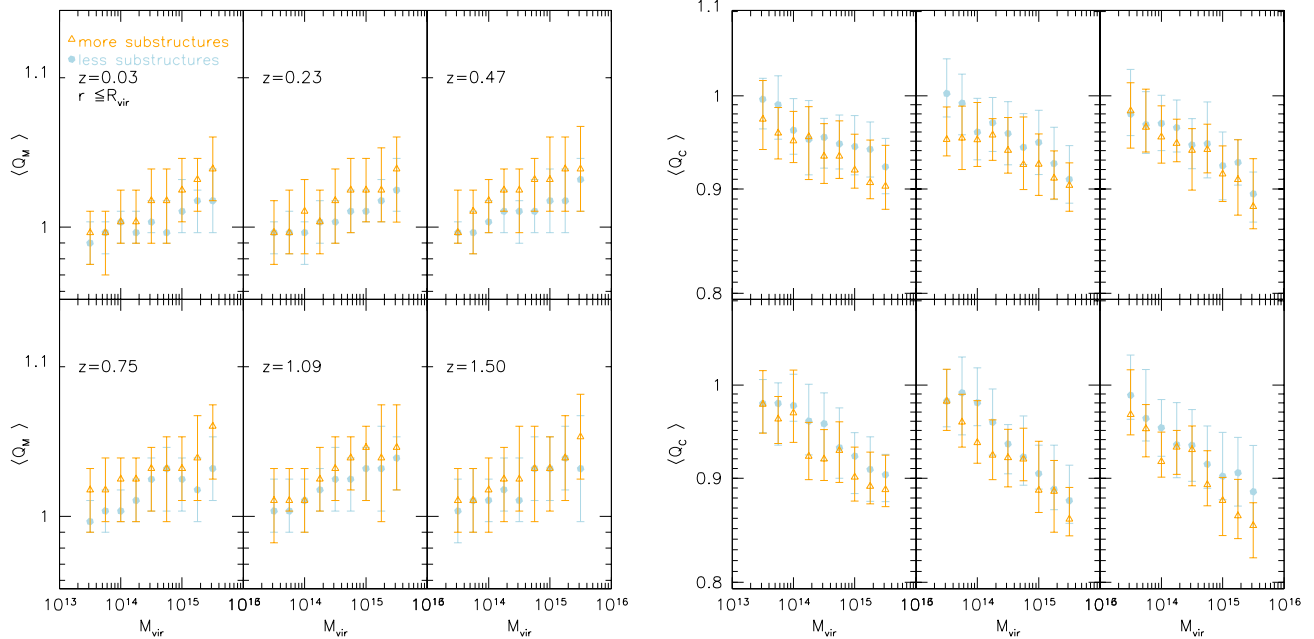


**Figure 6.** Median rescaled mass (*left panels*) and concentration (*right panels*) estimates as a function of the halo mass for the SPHwBCG subsamples with more (open triangles) and less (filled circles) substructures. The error bars correspond the first and the third quartile.

assumed to be spherical and with a BCG at their centres. From the figure we notice that, while the estimated masses are larger than the true ones for the substructured sample than for the unstructured, the opposite is valid for the estimated concentrations.

### 3.2 Triaxial Haloes

The spherical approximation used to describe the halo matter density distribution is far from being realistic. Different studies based on numerical simulations showed that the halo shape is triaxial (Sheth et al. 2001; Jing & Suto 2002;



Kazantzidis et al. 2004). This is because during the collapse phase a halo is influenced by its surrounding tidal field which stretches and shears its matter distribution. Various observations of galaxy clusters, both in optical and in X-rays, have confirmed this picture and have revealed that a discrete number of X-ray-selected clusters present also their major axis elongated along the line of sight. This condition is typically sufficient, but not necessary, to cause, in their optical images, the presence of very distorted gravitational arcs and large Einstein rings, and also a discrepancy between galaxy cluster masses and concentrations determined from X-ray and gravitational lensing observations. Combining X-ray, weak and strong lensing observations, Morandi et al. (2010) have proposed a method to determine the galaxy cluster elongation along the line of sight (with an error of the order of 5%) and reconcile the discrepancy of the mass and the concentration estimates. The observational estimate of the elongation of the cluster halo along of the line of sight is very challenging and only possible for clusters that are very massive and located at low redshifts.

Let us now consider the case of a triaxial prolate or oblate halo, and define its axes as  $e_a$ ,  $e_b$  and  $e_c$ ; if the halo is spherical in the plane of the sky ( $e_a = e_b = 1$ ) and  $e_c$  is parallel of the line of sight, the convergence of the halo will be defined as:

$$\Sigma(x, y) = e_c \int_{-\infty}^{\infty} \rho(x, y, \zeta') d\zeta', \quad (15)$$

with  $\zeta' \equiv \zeta/e_c$ .

In MOKA we have included the model proposed by Jing & Suto (2002) to describe the main halo ellipticity, according to which the stellar component of the BCG and the subhalo spatial distribution are also perturbed. Using the axial ratio probability distributions we estimate  $e_a$ ,  $e_b$  and  $e_c$ , requiring that  $e_a e_b e_c = 1$ . Once the axial ratios are known, we randomly orient the halo choosing a point on a sphere identified by its azimuthal and elevation angles; according to this we rotate the halo ellipsoid and deform the convergence map. The elongation  $e_z$  represents the largest component of the ellipsoid axes projected along the line of sight.

In Figure 7, we show  $Q_M$  and  $Q_c$  as a function of the host halo mass, obtained by fitting the convergence profiles of the ELLwBCG sample up to  $R_{vir}$  and at six different redshifts. In fitting the convergence profile of the triaxial clusters, and in estimating mass and concentration, we proceed in two ways: (i) in the first case we make use directly of  $\kappa_{NFW}(r)$  from equations 11 and 13 and minimize  $\chi^2(M_{fit}, c_{fit})$  (eq. 14); (ii) in the second case we multiply  $\kappa_{NFW}(r)$  by  $e_z$ , the elongation of the halo along the line of sight (assumed without error), and estimate  $M_{fit}$  and  $c_{fit}$  again minimizing  $\chi^2$ . We refer to this last case as mass and concentration estimates corrected for elongation.

In the left panels of Fig. 7, we notice that the mass bias, found also by Meneghetti et al. (2011) and Rasia et al. (2012) - who fitted the tangential shear profile using simulated observations of galaxy clusters - almost disappears when we correct for elongation. In the right panels we show the results for the concentration. When we do not include the elongation in the calculations, both  $Q_M$  and  $Q_c$  are underestimated of 10 – 20%. Conversely, when we correct for elongation, the mass estimate is unbiased, while the resulting concentration is still slightly underestimated, since  $Q_M$

and  $Q_c$  are not independent of each other, considering that  $c_{vir} \sim M_{vir}^{1/3}$  they do not scale in the same way but as:  $\Delta Q_c = (\Delta Q_M)^{1/3}$ .

To discuss the importance of the range used to fit the convergence profile, in Figure 8 we show the median rescaled mass and concentration as a function of the true halo mass, when the fit of the convergence profile is done on different radial ranges. These are the same chosen for the analysis presented in Fig. 5. Again we note that the error bars become larger when fitting on a narrower radial range. In the figure we do not observe significant differences in the radial ranges  $[0, 1]R_{vir}$ ,  $[0, 0.5]R_{vir}$ ,  $[0.1, 1]R_{vir}$  and  $[0.25, 1]R_{vir}$ . Fitting the most central region, where the BCG dominates the convergence profile, the masses and the concentrations are slightly underestimated and overestimated, respectively. As show for the spherical case, fitting the profile outside  $0.5R_{vir}$  we overestimate both the halo mass and concentration with not much difference between the two cases in which we do or do not correct the convergence profile for elongation.

Fitting the profile without any assumption on the value of the elongation creates a strong bias in the mass estimates due to the elongation along the line of sight. This can be better quantified dividing the halo sample, in each mass bin according to the level of elongation, in more and less elongated systems. In Figure 9 we again show the median masses and concentrations as a function of the true mass for the samples of haloes with large and small elongation. The separation of haloes in these two classes was made by measuring the median elongation  $\langle e_z \rangle$  in each mass bin. We define as “less elongated” haloes those with  $e_z < \langle e_z \rangle$ , and vice-versa. This analysis shows that the two samples have a large differences both in mass (left panel) and in concentration (right panel) of about 35 – 40%. We can summarize that while more and less substructured haloes have a difference in the estimates of the order of few percent, the estimates between more and less elongated haloes can differ up to more than 50%, in the case of very massive clusters.

This can originate very important systematics when trying to recover cosmological information from the mass and concentration estimates based on lensing analysis without taking into account possible projection effects (Sereno & Zitrin 2012; Coe et al. 2012).

#### 4 COSMOLOGY FROM THE $C - M$ RELATION OF A WIDE FIELD SURVEY

Several studies aimed at constraining cosmological parameters by measuring the  $c - M$  relation of galaxy clusters. For example, Ettori et al. (2010) used a sample of 44 X-ray luminous clusters observed with XMM-Newton. They measured the masses and the concentrations by assuming spherically symmetric X-ray emitting gas distributions in hydrostatic equilibrium with the cluster gravitational potentials, which are modeled by NFW functionals. By comparing with theoretical  $c - M$  relations, they constrain the degeneracy between  $\Omega_m$  and  $\sigma_8$ . Checking the consistency of the observed cluster  $c - M$  relation with the theoretical expectations in the framework of the  $\Lambda$ CDM cosmology is also one of the goals of the ongoing CLASH Multi-Cycle-Treasury program of the Hubble Space Telescope (?). Interesting results are

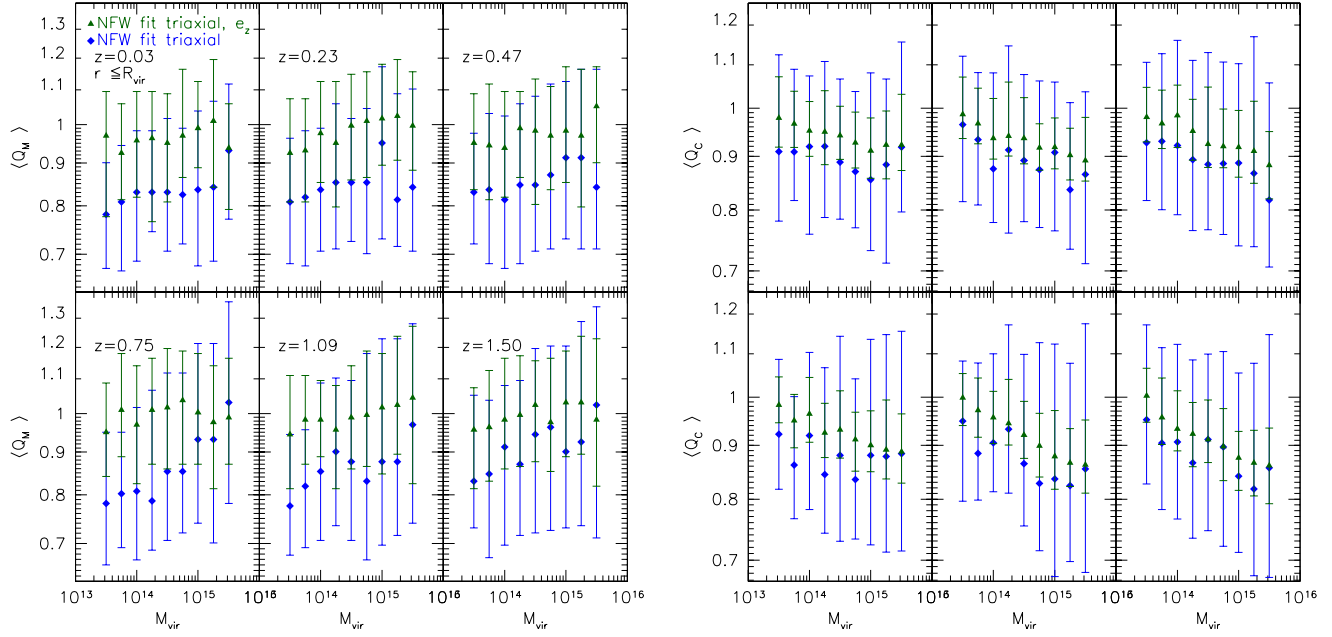


**Figure 7.** Median rescaled mass (*left panels*) and concentration (*right panels*) estimates as a function of the halo mass, for triaxial substructured haloes with BCG, located at six different redshifts. The mass of each halo has been estimated best fitting the spherical averaged convergence profile of each halo, up to the virial radius  $R_{vir}$ , with a NFW function varying both the mass and the concentration. The two different data points refer to two cases in which the fit has been performed not knowing (filled diamonds) or knowing (filled triangles) the halo elongation along the line of sight. The error bars enclose the first and the third quartiles of the distribution in each mass bin.

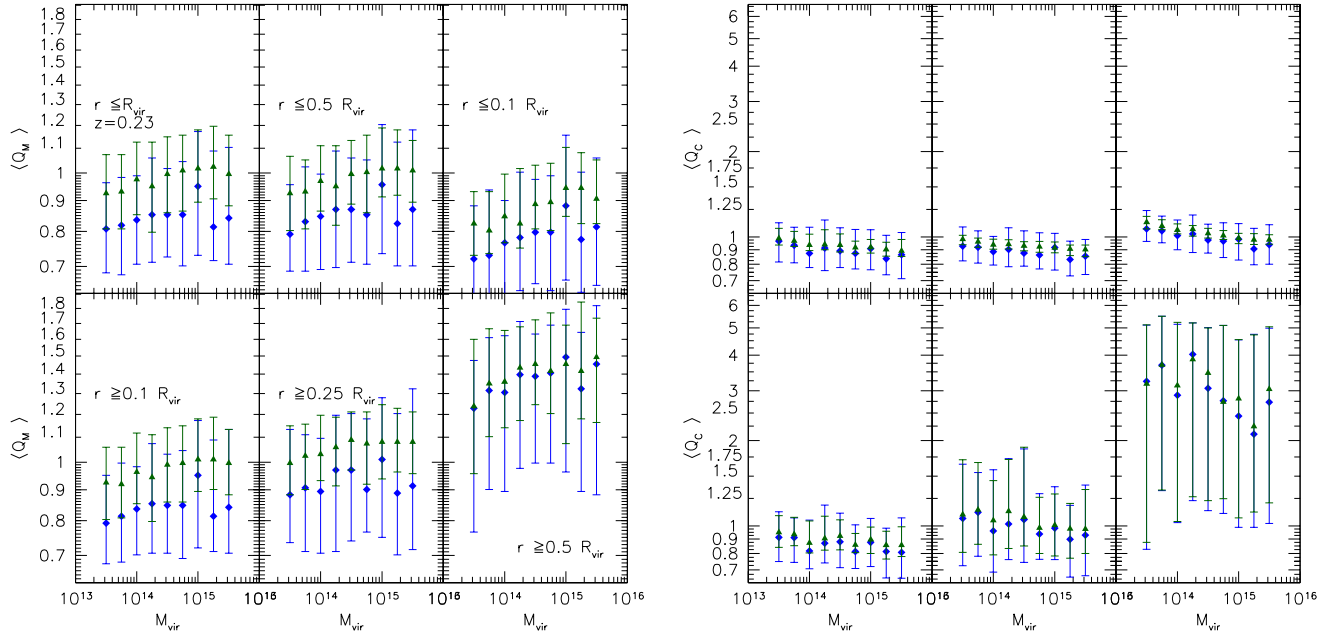


**Figure 8.** Median rescaled mass (*left panels*) and concentration (*right panels*) estimates as a function of the halo mass, for triaxial and substructured haloes with BCG located at redshift  $z = 0.23$ . The top panels show the relation obtained fitting the profile without any assumption on the value of the elongation up to  $R_{vir}$ ,  $0.5R_{vir}$  and  $0.1R_{vir}$ ; while the bottom ones from  $R_{vir}$  down to  $0.1R_{vir}$ ,  $0.25R_{vir}$  and  $0.5R_{vir}$ . The different data points and error bars are the same as in the Figure 7.

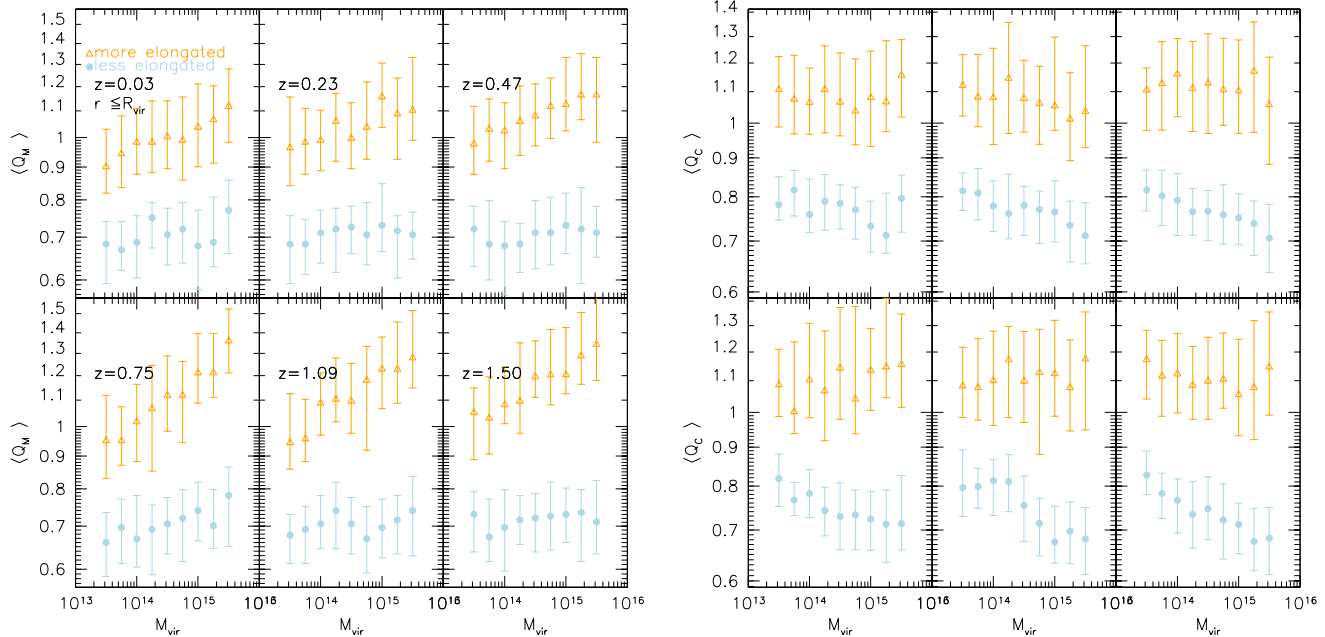


**Figure 9.** Median rescaled mass (*left panels*) and concentration (*right panels*) estimates as a function of the hist halo mass, for the ELLwBCG sample by fitting the profile without any assumption on the value of the elongation using a NFW-funtion. In each mass bin we divided the haloes in more (open triangles) and less (filled circles) elongated along the line of sight. The various panels show the relation at six different redshifts.

emerging from these analyses, whose significance is however limited by the relatively small sizes of the cluster samples.

The situation is going to significantly improve in the near future. Indeed, several optical surveys are planned, which will deliver high quality data suitable for the weak lensing analysis of large samples of galaxy clusters (e.g. KiDS, DES<sup>2</sup>, LSST, Kuyken (2010); LSST Science Collaborations et al. (2009)). In particular, in the wide survey that will be operated by the Euclid mission, several dozen of thousands of galaxy clusters will be detectable up to redshift 2. Now, we attempt to quantify the robustness of the cosmological constraints that it will be possible to derive from the analysis of such large cluster samples.

The first step towards our goal is to model a cluster selection function. In this work, we make the simple assumption that cluster detections will be not contaminated above a constant mass limit of  $5 \times 10^{13} M_{\odot}/h$  for  $z < 0.4$  and  $1.5 \times 10^{14} M_{\odot}/h$  for  $z \geq 0.4$ . This reflects the fact that at high redshift we tend to select only massive clusters. More detailed selection functions should be derived for specific surveys, depending on their depth, observing bands, etc. The mass limit used in this work is consistent with the analytical estimates for the EUCLID photometric selection function (Laureijs et al. 2011). We use the selection function in combination with the Sheth & Tormen (1999) mass-function to generate a population of cluster-sized dark matter halos reproducing the mass and redshift distributions expected in the context of a corresponding  $\Lambda$ CDM cosmology (see Sect. 1 for the exact choice of the cosmological parameters). We use these halos to populate a light-cone corresponding to a sur-

vey area of 15000 sq. degrees. The sampled volume extends from  $z = 0.03$  and  $z = 1.5$  and is subdivided in slices equally spaced in  $\log(1+z)$ . We further use the Zhao et al. (2009)  $c - M$  relation, including a redshift dependent log-normal scatter as shown in Figure 1, to assign a concentration to each halo.

As we discussed in the previous sections, projection effects introduce substantial biases in the measurements of masses and concentrations. Such biases can be quantified using the simulations done with the MOKA code. More specifically, for any input mass and redshift, we can use the simulations to derive the expected distribution of the measured masses and concentrations, assuming they are obtained by fitting the two-dimensional mass profiles of triaxial halos. In the left and right panels of Figure 10, we show how the rescaled masses and concentrations are expected to change as a function of the halo virial mass  $M_{vir}$ . The results were obtained by combining the ELLwBCG samples at 16 different redshifts. Triangles and diamonds refer to the cases where the projected mass profiles were fitted with and without correcting for the elongation along the line of sight (Eq. 15 with  $e_c = e_z$ ). They indicate the median rescaled masses and concentrations in each mass bin. The error-bars correspond to the inter-quartile ranges of the distributions in the mass bins. We performed linear least-squares fits to the data points and we measured the relations given by short- and the long-dashed lines in each panel. We can explicit these relations as

$$\log(Q_M) = 0.025 \log(M_{vir}) - 0.433; \text{rms} = 0.094 \quad (16)$$

$$\log(Q_C) = -0.018 \log(M_{vir}) + 0.212; \text{rms} = 0.081 \quad (17)$$

when no correction for elongation is applied. When the fit

<sup>2</sup> <http://www.darkenergysurvey.org>

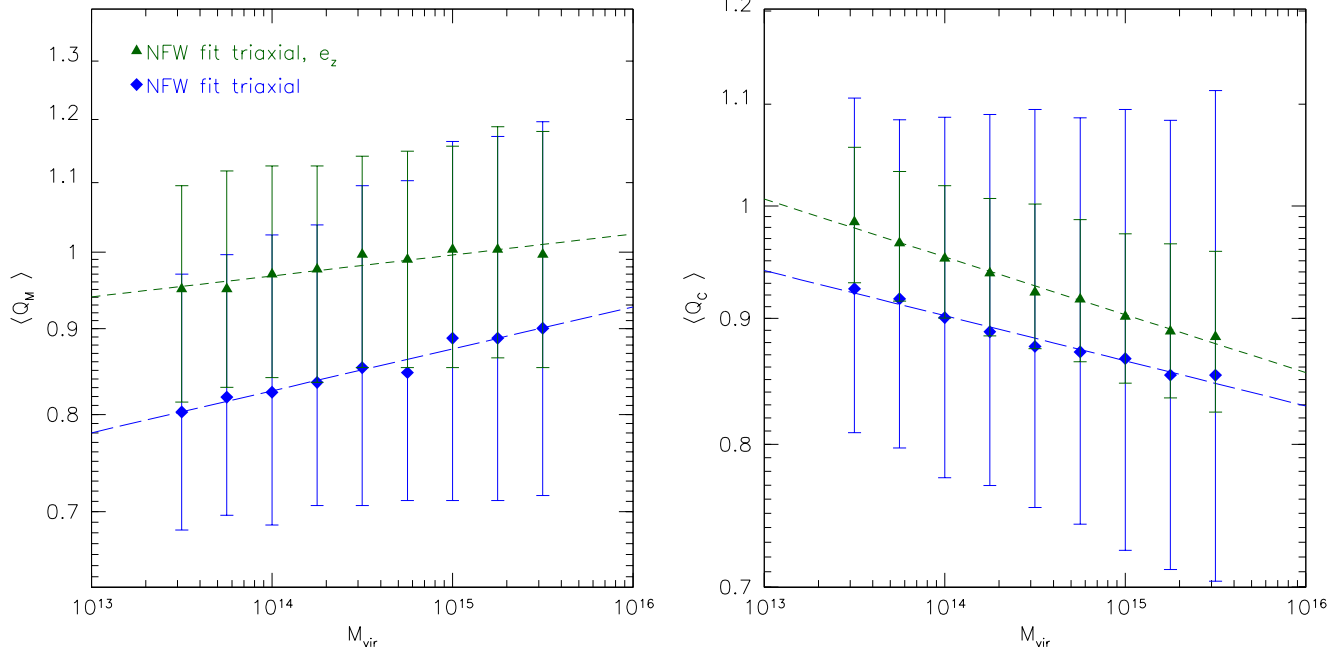


**Figure 10.** Median rescaled mass (*left panel*) and concentration (*right panel*) as a function of the true halo mass, combining the results of 16 redshift slices between  $z = 0.03$  up to  $z = 1.5$ , for the ELLwBCG sample. Diamonds and triangles show the results for the NFW fits without and with correction for elongation, respectively. The error bars show the first and the third quartile of the distribution. The long and short-dashed lines show the least-squares fits to the data.

is done correcting for  $e_z$ , we obtain

$$\log(Q_M) = 0.013 \log(M_{vir}) - 0.190; \text{rms} = 0.066 \quad (18)$$

$$\log(Q_C) = -0.023 \log(M_{vir}) + 0.308; \text{rms} = 0.029 \quad (19)$$

We use these equations and their r.m.s. to assign to each halo in the light-cone values of  $Q_M$  and  $Q_c$ . Therefore, we compute the “biased” masses and concentrations as

$$M_{fit} = M_{true} \times Q_M \quad (20)$$

$$c_{fit} = c_{true} \times Q_c. \quad (21)$$

Once we have realistically included the biases caused by projection effects, we can proceed to measure the halo  $c_{fit} - M_{fit}$  relation and use it to constrain the cosmological parameters. In particular, in this section we focus on  $\sigma_8$ ,  $\Omega_m$ , and  $w$ .

We show in Figure 11 the results obtained in six different redshift bins ranging between  $z = 0.03$  (upper-left panel) and  $z = 1.5$  (bottom-right panel). The solid black curve show the input  $c - M$  relation by Zhao et al. (2009). As usual, the green triangles and the blue diamonds indicate the concentrations and masses recovered with and without correcting for elongation. As we can see, the diamonds are biased lower than the triangles with respect to the Zhao et al.  $c - M$  relation. These reflect the results shown in Figure 10, where we see that correcting for  $e_z$  generally allows to recover the correct input mass, but it leads to a still slightly lower estimate of the cluster concentration. These results seem to indicate that a correction for elongation, as given in Eq. 15 with  $e_c = e_z$ , should be applied to the cluster mass. As explained before when we correct for elongation, the mass estimate is unbiased, while the resulting concentration is corrected but not enough, since  $Q_M$  and  $Q_c$  are

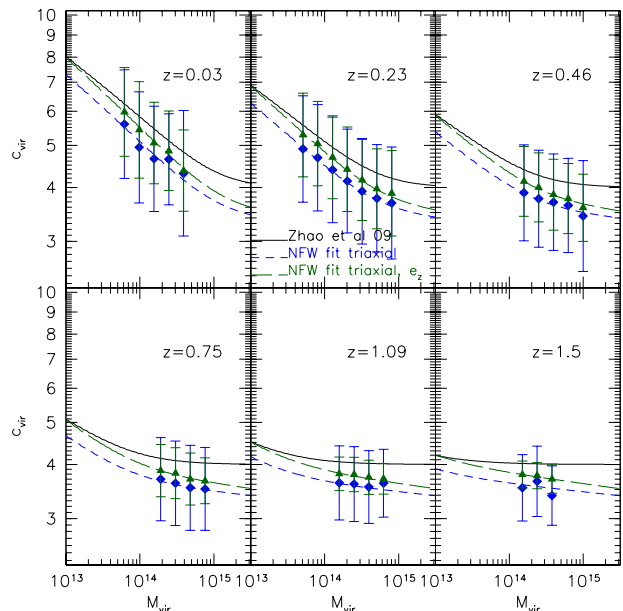


**Figure 11.** Concentration-mass relations at six different redshifts. The different points show the average concentrations and r.m.s. in different mass bins. The solid curve indicate the input  $c - M$  relation of Zhao et al. Diamonds and triangles show the results obtained by fitting the profiles without and with correction for elongation. The short and the long-dashed lines are the functionals that best fit the data (see text for more details).

not independent of each other, considering that  $c_{vir} \sim M_{vir}^{1/3}$  they do not scale in the same way but as:  $\Delta Q_c = (\Delta Q_M)^{1/3}$ .

We fit the triangles and the diamonds with functions of the kind

$$c_{2D}(M) = c_{3D}(M) \times N M^\lambda, \quad (22)$$

where  $c_{3D}$  is the input  $c-M$  relation (in our case the model by Zhao et al. (2009)) and we find that they are well fitted by the following functional forms:

$$c_{2D}(M) = c_{3D}(M) \times \begin{cases} 1.630 M^{-0.018}, & \text{(short - dashed)} \\ 2.033 M^{-0.023}, & \text{(long - dashed)}, \end{cases} \quad (23)$$

respectively. Finally, we use the recovered  $c_{fit} - M_{fit}$  relations to constrain the cosmological parameters. To do so, we compare them to corresponding  $c-M$  relations of Zhao et al. recalculated by varying the cosmological parameters. In this experiment, we vary only two of the investigated cosmological parameters simultaneously, while we keep the third fixed and equal to value used in our simulations. The purpose of this experiment is to quantify the degeneracies between cosmological parameters when constraining them using the  $c-M$  relation. If the couple of parameters which is changed is  $(\Phi, \Psi)$ , we define the  $\chi^2$  variable as

$$\chi^2(\Phi, \Psi) = \sum_j^{redshifts} \sum_i^{N_{mass\ bin}} \frac{\{\log[c_{fit,i}(z_j)] - \log[c_{model}(M_{fit,i}, z_j|\Phi, \Psi)]\}^2}{\sigma_{\log c,i}^2} \quad (24)$$

where  $\sigma_{\log c,i}$  represents the concentration *rms* in a given mass bin. Then, we find the couples of cosmological parameters,  $(\bar{\Phi}, \bar{\Psi})$ , that minimize  $\chi^2$ .

In Figure 12, we show the 1, 2, and  $3\sigma$  confidence levels for the couples of cosmological parameters  $(\sigma_8, w)$  (top panels),  $(w, \Omega_m)$  (middle panels), and  $(\sigma_8, w)$  (bottom panels). The results refer to a 15000 sq. degrees survey, combining measurements of the  $c-M$  relation in 16 redshift bins between  $z = 0.03$  and  $z = 1.5$ . In the left panels, we fit the input  $c-M$  relation, adding only a log-normal scatter in  $c_{vir}$ . As expected, we recover the input sets of cosmological parameters, corresponding to the  $\Lambda$ CDM cosmological model. In the middle column, we use the  $c_{fit} - M_{fit}$  relation measured without applying any correction for elongation. In this case, the  $c-M$  relation is best fitted by models with lower  $\sigma_8$  and lower  $\Omega_m$  when we fix  $w = -1$  (upper panel). Keeping  $\sigma_8 = 0.809$  (middle panel), the results are sensitive to  $\Omega_m$ , and values of  $w$  lower than  $-1$  are preferred (phantom dark energy). In both upper and middle panels, however, the input cosmological parameters are outside the  $3\sigma$  of the recovered sets of parameters. Fixing  $\Omega_m = 0.272$  (bottom panel), the input values of  $\sigma_8$  and  $w$  are outside the measurements. The right panels refer to the case where concentrations and masses are recovered by correcting for the true halo elongations using Eq. 15 with  $e_c = e_z$ . The results of the fit in this case are qualitatively similar to those shown in the panels in the middle column, but the offset between recovered and input cosmological parameters is slightly weaker.

In Table 2, we quantify the degeneracy between the couples of cosmological parameters estimated from the

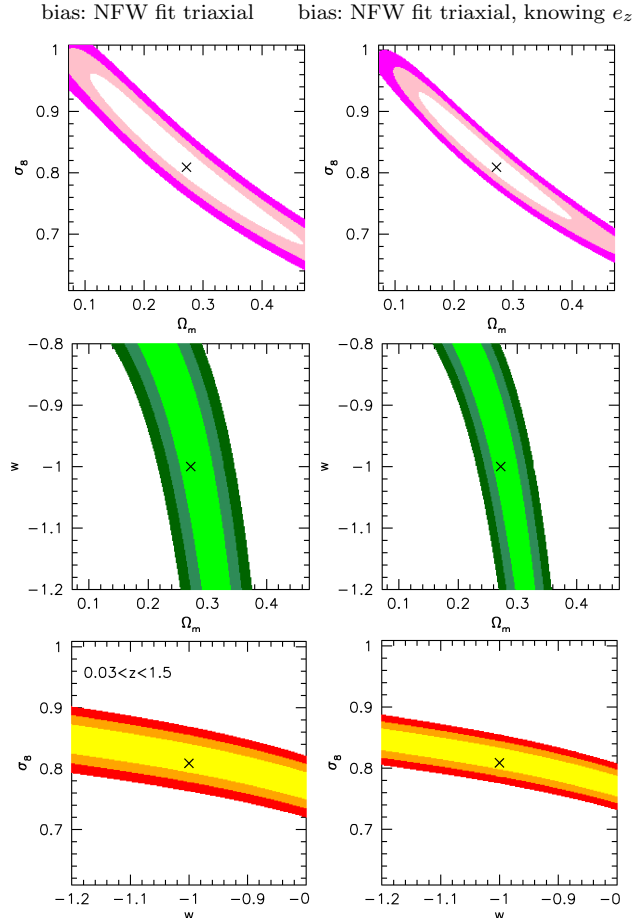


**Figure 13.** 1, 2 and  $3\sigma$  confidence levels in the planes  $(\sigma_8, \Omega_m)$  (top panels),  $\sigma_8 - \Omega_m$ , and  $\sigma_8 - w$  (bottom panels). Here, the relations given in Eq. 23 are used to correct the biases on the  $c-M$  relations..

concentration-mass relation. Results are reported for  $3 - \sigma$  and  $1 - \sigma$  (in parentheses) confidence limits.

In Figure 13 we present again the confidence levels for the cosmological parameters obtained when fitting the  $c-M$  relations in the cases without and with correction for elongation (left and right panels, respectively). In these cases, however, we used the relations in Eq. 23 to correct for the biases in the  $c-M$  relations. As expected the input cosmological models are now perfectly recovered within  $1\sigma$ .

## 5 SUMMARY AND CONCLUSIONS

In this work, we studied how well the three-dimensional masses and concentrations of galaxy clusters are recovered from their projected mass distributions. We did this by fitting the convergence profiles of a large sample cluster-sized halos generated with the publicly available code MOKA adopting NFW-functionals. We investigated several sources of possible biases in the measurements. In particular, we studied the biases introduced by the presence of 1) substructures of different masses, 2) a massive galaxy at the center of clusters, and 3) cluster triaxiality. Additionally, we considered the systematics related to the choice of the radial range where the projected mass profile is fitted. We also

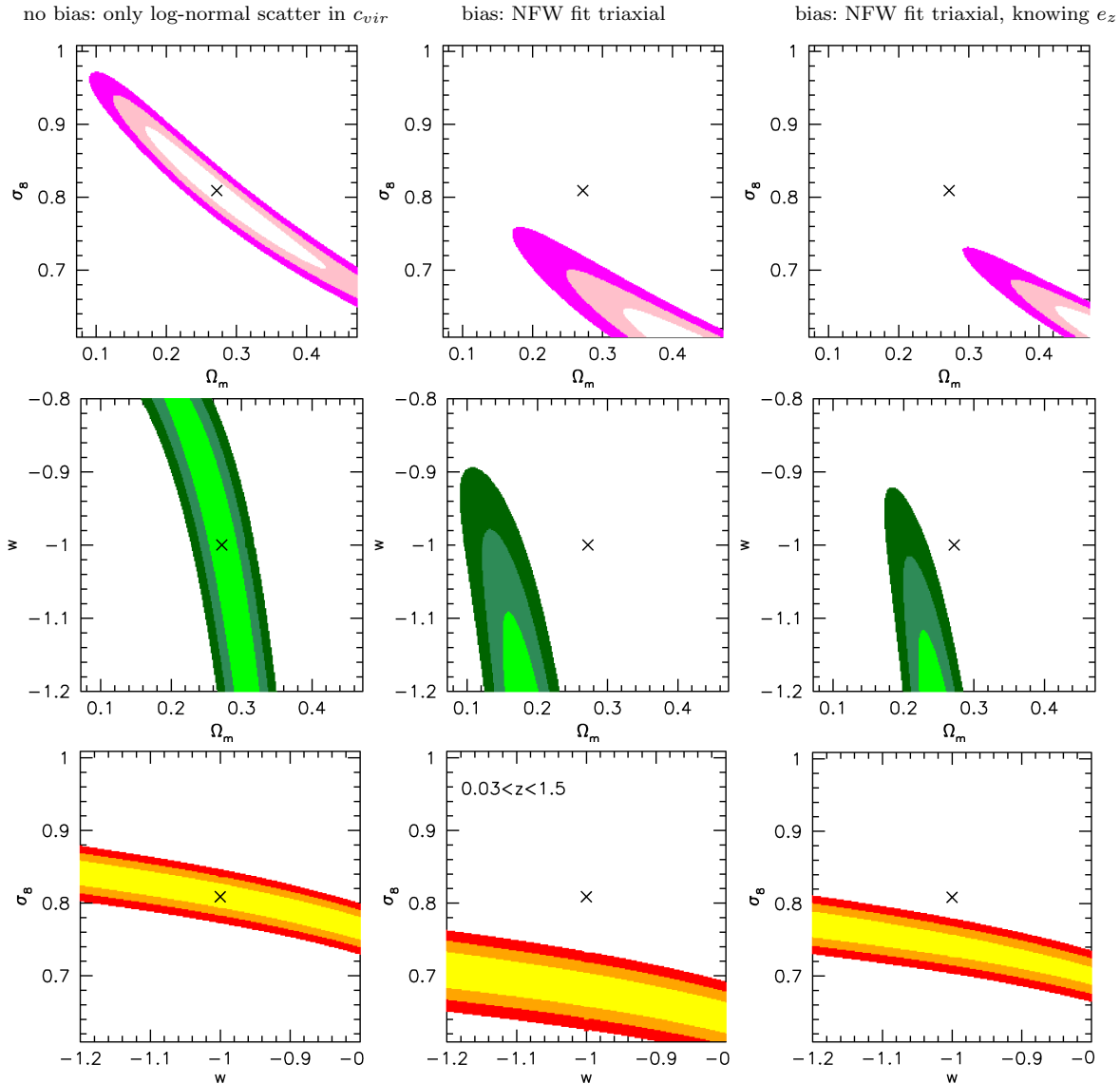


**Figure 12.** 1, 2 and 3  $\sigma$  confidence levels in the planes  $\sigma_8, \Omega_m$  (top panels) and  $\sigma_8, w$  (bottom panels). The results refer to a 15000 sq. degrees survey, combining measurements of the  $c - M$  relation in 16 redshift bins between  $z = 0.03$  and  $z = 1.5$ . In the left panels, we fit the input  $c - M$  relation, adding only a log-normal scatter in  $c_{vir}$ . In the middle column, we use the  $c_{fit} - M_{fit}$  relation measured without applying any correction for elongation. Finally, the right panels refer to the case where, concentrations and masses are recovered by correcting for the true halo elongations using Eq. 15 with  $e_c = e_z$ . The true sets of cosmological parameters are indicated by the black crosses ( $\Lambda$ CDM cosmological model).

**Table 2.** Degeneracy between cosmological parameters estimated from the concentration-mass relation. The subscript (0) indicates the input parameters, which correspond to a  $\Lambda$ CDM cosmological model ( $\Omega_{m,0} = 0.272$ ,  $w_0 = -1$  and  $\sigma_{8,0} = 0.809$ )

parameters	$\alpha$	$\beta$
$\frac{\sigma_8}{\sigma_{8,0}} = \beta \left( \frac{\Omega_m}{\Omega_{m,0}} \right)^\alpha$	-0.235 (-0.265)	0.983 (0.994)
$\frac{w}{w_0} = \beta \left( \frac{\Omega_m}{\Omega_{m,0}} \right)^\alpha$	1.082 (1.112)	-1.019 (-1.013)
$\frac{\sigma_8}{\sigma_{8,0}} = \beta \left( \frac{w}{w_0} \right)^\alpha$	0.231 (0.231)	0.999 (1.000)

investigated how the mass and concentration measurements change by adding a correction factor that takes into account the cluster elongation along the line-of-sight. Finally, we investigated the robustness of cosmological constraints derived from the concentration-mass relation measured in large samples of galaxy clusters.

Our findings can be summarized as follows:

- by distributing substructures in spherically symmetric cluster halos, we found that the concentrations recovered from cluster convergence profiles are on average biased low by  $\sim 5 - 6\%$ . This bias tends to increase as a function of mass, because the most massive haloes are expected to possess a larger fraction of their mass in substructures. These substructures have an even smaller effect on the cluster mass estimates, which differ from the input masses by just a few percent;

- the presence of massive galaxies at the cluster center generally causes tiny over-estimate of the mass, when the convergence profile is fitted with simple NFW functionals. Such over-estimate is slightly more evident for small-mass halos, where it is of order few percent;

- the above mentioned results have little dependence on redshift, while they depend more significantly on the radial range chosen to perform the fit of the convergence profile. More precisely, the effects of massive central galaxies are remarkable if the fit is restricted to the very inner region of the clusters ( $r < 0.1R_{vir}$ ). In this case, the cluster mass can be under-estimate by up to 10%, while the concentration can be over-estimated by the same amount;

- modeling the halo triaxiality following the Jing & Suto (2002) prescription and assuming random halo orientations, the three-dimensional masses recovered from the fit of the convergence profiles are on average biased low by  $\sim 10-20\%$ . However, for more massive clusters the mass bias is not larger than 10%, as also found by Meneghetti et al. (2011); Rasia et al. (2012) using the tangential shear profile of simulated galaxy clusters. This bias is larger than what found by Corless & King (2009) whose triaxial clusters are constructed without substructures and with a different model for the axial ratios  $e_a/e_c$  and  $e_b/e_c$  (Shaw et al. 2006) imposing  $e_a e_b e_c = 1$ , as we do, but with  $e_a < e_b < e_c = 1$ . We explained such under-estimate of the mass as due to a larger probability to observe clusters elongated on the plane of the sky than along the line-of-sight and to the combined effects of triaxiality and presence of substructures – as quantified and discussed in Section 3. We notice that in this case, we also measure low concentrations, this bias in halo properties estimates has also been studied and discussed in several other studies (Clowe et al. 2004; Oguri et al. 2005; Gavazzi 2005; Corless & King 2007);

- introducing a correction for elongation multiplying the convergence by  $e_z$ , we found that the bias in mass can be removed. This correction also moves  $Q_c$  toward unity but still keeping a small negative bias;

- by simulating a cluster survey covering an area of 15000 sq. degrees, we estimated that triaxiality and substructure induced biases on the 3D  $c-M$  relation, that would translate into biases on the values of cosmological parameters like  $\sigma_8$ ,  $\Omega_m$ , and  $w$ , if no correction for elongation is applied. The biases decrease when correcting for elongation.

We conclude that, in order to use the cluster  $c - M$

relation, measured from the cluster projected density profiles as they might be determined by means of the cluster lensing signal (see e.g. Coe et al. 2012; Sereno & Zitrin 2012), to constrain the cosmological parameters, it is necessary to take into account possible biases due to substructures and halo triaxiality. This can be done introducing a 2D  $c-M$  relation correcting the 3D one for projection effects.

## ACKNOWLEDGEMENTS

We thank the anonymous referee for his useful comments that helped to improve the presentation and the discussion of our results.

We also thank Giulia Despali, Ravi K. Sheth and Giuseppe Tormen for useful comments and interesting suggestions.

We acknowledge financial contributions from contracts I/009/10/0, EUCLID-IC phase A/B1, PRIN-INAF 2009, ASI-INAF I/023/05/0, ASI-INAF I/088/06/0, ASI I/016/07/0 COFIS, ASI Euclid-DUNE I/064/08/0, ASI-Uni Bologna-Astronomy Department Euclid-NIS I/039/10/0 and PRIN MIUR dark energy and cosmology with large galaxy surveys. CG's research has been partially supported by the project GLENCO, funded under the Seventh Framework Programme, Ideas, Grant Agreement n. 259349.

## APPENDIX A: ADIABATIC CONTRACTION

The presence of a dissipative baryonic component influences the dark matter distribution. This is because cold baryons that settle at the host halo centre act contracting the dark matter. Blumenthal et al. (1986) described the adiabatic contraction analytically, finding a good agreement with numerical simulations. However the halo contraction, as measured in numerical simulations with gas physics, may depend on the parameters that model the star formation processes and the gas physics. In these cases, the evolution of the central density may also be affected by spurious numerical effects due to two-body scattering of massive particles. Also the differences in some models can be due to a higher density threshold for star formation, for example in the case in which the supernova energy release is more concentrated and creates rapid potential fluctuations near the center. The model by Blumenthal et al. (1986) assumes that a spherically symmetric halo can be thought of as a sequence of concentric shells, made of particles on circular orbits, which homogeneously contract while conserving the angular momentum. The initial and final density profiles – characterized by an initial radius  $r_i$  and a final radius  $r_f$ , when a central galaxy is present – are related by

$$r [M_{BCG}(r) + M_{DM,f}] = r_i M_{DM,i}(r_i), \quad (A1)$$

where

$$M_{DM,f} = M_{DM,i} (1 - f_{cool}), \quad (A2)$$

and  $f_{cool}$  is the baryon fraction in the halo that cools to form the central galaxy. To solve the adiabatic-contraction equation, we need to derive  $r$  from equation (A1). When

the stellar density distribution is described by a Hernquist model we can read:

$$f_{cool}r^3 + (r + r_h)^2 [(1 - f_{cool})r - r_i] m_i(r_i) = 0, \quad (\text{A3})$$

while for a Jaffe model we have:

$$[f_{cool} + m_i(r_i)(1 - f_{cool})] r^2 + m_i(r_i)(r_j - f_{crj} + r_i)r + r_i r_j m_i(r_i) = 0 \quad (\text{A4})$$

where  $r_h$  and  $r_j$  represent respectively the scale radius of the two models. The two equations have a single positive real root. We recall that  $m_i$  in the previous equations defines the initial mass profile normalized by the halo virial mass. From the equation above results that the presence of a dissipative baryonic component contracts the dark matter distribution.

The model we described above, and used to model the dark matter contraction in our haloes, is often defined as standard adiabatic contraction (SAC). Gnedin et al. (2011) have defined a modified adiabatic contraction (MAC) model that takes into account the results from numerical simulations in which gas physics and merging events are included. They argue that the MAC model gives excellent predictions to the data, while the SAC model tends to overestimate the dark matter content toward the halo centre. We also stress that the adiabatic contraction observed in numerical simulations depends directly on the adopted parameters. Cosmological simulations performed by different authors, with very different codes and physics inputs, agree that the contraction effect is present, but at a weaker level than suggested by the SAC model and with a significant variation from system to system and from input model to input model.

Figure A1 shows the median ratio of the best fit estimate of the mass (crosses) and the concentration (filled circles) between the run with (ELLwBCGwADC) and without adiabatic (ELLwBCGwADC) contraction as a function of the host halo mass. We notice that in systems where the ratio between the BCG mass and the virial mass is higher (small systems) the contraction tends to increase the concentration up to a 10%, while for haloes where  $M_{BCG}/M_{vir}$  is lower (larger systems) the ratio approaches to unity. From the figure we also notice that the ratio between the two mass estimates is influenced by the adiabatic contraction by only few percents.

In the Figure, the two solid curves, that consider the case of a BCG following a Hernquist (1990) profile, correspond

$$\log\left(\frac{M_{fit,wADC}}{M_{fit,nADC}}\right) = \exp[-(\log M_{vir} - 13.58)]/88.80, \quad (\text{A5})$$

$$\log\left(\frac{c_{fit,wADC}}{c_{fit,nADC}}\right) = \exp[-(\log M_{vir} - 14.12)]/51.04, \quad (\text{A6})$$

respectively, while the dashed curves, that consider the case of a BCG following a Jaffe (1983) model correspond:

$$\log\left(\frac{M_{fit,wADC}}{M_{fit,nADC}}\right) = \exp[-(\log M_{vir} - 13.95)]/89.72, \quad (\text{A7})$$

$$\log\left(\frac{c_{fit,wADC}}{c_{fit,nADC}}\right) = \exp[-(\log M_{vir} - 14.53)]/49.04, \quad (\text{A8})$$

which best fit the data points. These equations can be used to modify the concentration-mass relation measured in pure dark matter simulation to include the effects of a dissipative stellar component at the host halo centre.

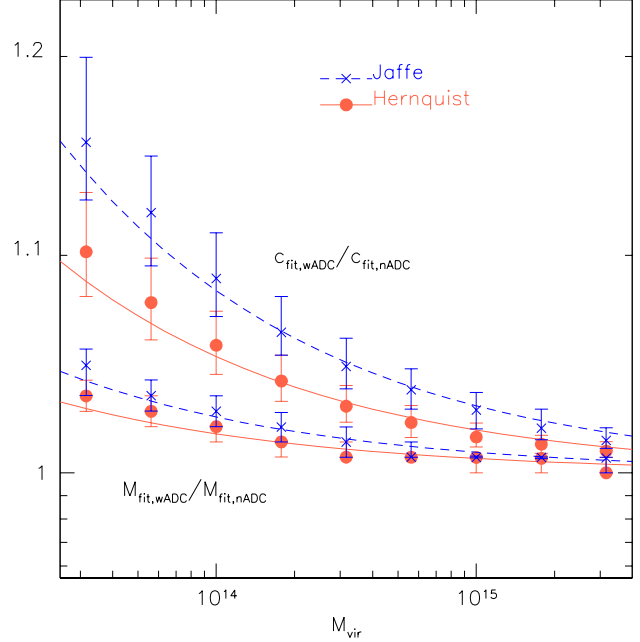


**Figure A1.** Median ratio between the concentration and mass estimates obtained from the simulations performed at  $z = 0.03$ , 0.23, 0.47, 0.75, 1.09 and 1.50 with and without the inclusion of the adiabatic contraction, as a function of the host halo mass. We show the results for the BCG following a Hernquist (1990) and a Jaffe (1983) profile. The error bars show the first and the third quartiles. The curves show the best fit to the data – see equations (A6) (A5) (A8) (A7).

## REFERENCES

- Andreon S., 2010, *MNRAS*, 407, 263  
Bahé Y. M., McCarthy I. G., King L. J., 2012, *MNRAS*, 421, 1073  
Bartelmann M., 1996, *A&A*, 313, 697  
Becker M. R., Kravtsov A. V., 2011, *ApJ*, 740, 25  
Becker M. R., McKay T. A., Koester B., Wechsler R. H., Rozo E., Evrard A., Johnston D., Sheldon E., Annis J., Lau E., Nichol R., Miller C., 2007, *ApJ*, 669, 905  
Bhattacharya S., Habib S., Heitmann K., 2011, *ArXiv e-prints*  
Blumenthal G. R., Faber S. M., Flores R., Primack J. R., 1986, *ApJ*, 301, 27  
Boylan-Kolchin M., Springel V., White S. D. M., Jenkins A., Lemson G., 2009, *MNRAS*, 398, 1150  
Clowe D., De Lucia G., King L., 2004, *MNRAS*, 350, 1038  
Coe D., Umetsu K., Zitrin A., Donahue M., Medezinski E., Postman M., Carrasco M., Anguita T., Geller M. J., Rines K. J., Diaferio A., Kurtz M. J., et al., 2012, *ArXiv e-prints*  
Conroy C., Prada F., Newman J. A., Croton D., Coil A. L., Conselice C. J., Cooper M. C., Davis M., Faber S. M., Gerke B. F., Guhathakurta P., Klypin A., Koo D. C., Yan R., 2007a, *ApJ*, 654, 153  
Corless V. L., King L. J., 2007, *MNRAS*, 380, 149  
Corless V. L., King L. J., 2009, *MNRAS*, 396, 315  
De Lucia G., Kauffmann G., Springel V., White S. D. M., Lanzoni B., Stoehr F., Tormen G., Yoshida N., 2004, *MNRAS*, 348, 333



- Dolag K., Bartelmann M., Perrotta F., Baccigalupi C., Moscardini L., Meneghetti M., Tormen G., 2004, *A&A*, 416, 853
- Eke V. R., Cole S., Frenk C. S., 1996, *MNRAS*, 282, 263
- Ettori S., Gastaldello F., Leccardi A., Molendi S., Rossetti M., Buote D., Meneghetti M., 2010, *A&A*, 524, A68+
- Ettori S., Morandi A., Tozzi P., Balestra I., Borgani S., Rosati P., Lovisari L., Terenziani F., 2009, *A&A*, 501, 61
- Fedeli C., 2011, *ArXiv e-prints*
- Gao L., Navarro J. F., Cole S., Frenk C. S., White S. D. M., Springel V., Jenkins A., Neto A. F., 2008, *MNRAS*, 387, 536
- Gao L., White S. D. M., Jenkins A., Stoehr F., Springel V., 2004, *MNRAS*, 355, 819
- Gavazzi R., 2005, *A&A*, 443, 793
- Giocoli C., Meneghetti M., Bartelmann M., Moscardini L., Boldrin M., 2012a, *MNRAS*, 421, 3343
- Giocoli C., Moreno J., Sheth R. K., Tormen G., 2007, *MNRAS*, 376, 977
- Giocoli C., Tormen G., Sheth R. K., 2012b, *MNRAS*, 422, 185
- Giocoli C., Tormen G., Sheth R. K., van den Bosch F. C., 2010a, *MNRAS*, 404, 502
- Giocoli C., Tormen G., van den Bosch F. C., 2008, *MNRAS*, 386, 2135
- Gnedin O. Y., Ceverino D., Gnedin N. Y., Klypin A. A., Kravtsov A. V., Levine R., Nagai D., Yepes G., 2011, *ArXiv e-prints*
- Gottloeber S., Yepes G., Wagner C., Sevilla R., 2006, *ArXiv Astrophysics e-prints*
- Hernquist L., 1990, *ApJ*, 356, 359
- Hoekstra H., 2003, *MNRAS*, 339, 1155
- Hoekstra H., Hartlap J., Hilbert S., van Uitert E., 2011, *MNRAS*, 412, 2095
- Jaffe W., 1983, *MNRAS*, 202, 995
- Jing Y. P., 2000, *ApJ*, 535, 30
- Jing Y. P., Suto Y., 2002, *ApJ*, 574, 538
- Kazantzidis S., Kravtsov A. V., Zentner A. R., Allgood B., Nagai D., Moore B., 2004, *ApJ*, 611, L73
- Keeton C. R., 2001, *ApJ*, 561, 46
- Komatsu E., Smith K. M., Dunkley J., Bennett C. L., Gold B., Hinshaw G., Jarosik N., Larson D., Nolte M. R., et al. 2011, *ApJS*, 192, 18
- Kuijken K., 2010, in Block D. L., Freeman K. C., Puerari I., eds, *Galaxies and their Masks Dark Haloes as Seen with Gravitational Lensing*. p. 361
- Lacey C., Cole S., 1993, *MNRAS*, 262, 627
- Laureijs R., Amiaux J., Arduini S., Auguères J. ., Brinchmann J., Cole R., Cropper M., Dabin C., Duvet L., et al. 2011, *ArXiv e-prints*
- LSST Science Collaborations Abell P. A., Allison J., Anderson S. F., Andrew J. R., Angel J. R. P., Armus L., Arnett D., Asztalos S. J., Axelrod T. S., et al. 2009, *ArXiv e-prints*
- Macciò A. V., Dutton A. A., van den Bosch F. C., 2008, *MNRAS*, 391, 1940
- Macciò A. V., Dutton A. A., van den Bosch F. C., Moore B., Potter D., Stadel J., 2007, *MNRAS*, 378, 55
- Meneghetti M., Argazzi R., Pace F., Moscardini L., Dolag K., Bartelmann M., Li G., Oguri M., 2007b, *A&A*, 461, 25
- Meneghetti M., Bartelmann M., Moscardini L., 2003, *MNRAS*, 346, 67
- Meneghetti M., Fedeli C., Zitrin A., Bartelmann M., Broadhurst T., Gottlöber S., Moscardini L., Yepes G., 2011, *A&A*, 530, A17+
- Meneghetti M., Rasia E., Merten J., Bellagamba F., Ettori S., Mazzotta P., Dolag K., Marri S., 2010b, *A&A*, 514, A93+
- Metcalf R. B., Madau P., 2001, *MNRAS*, 563, 9
- Morandi A., Pedersen K., Limousin M., 2010, *ApJ*, 713, 491
- Navarro J. F., Frenk C. S., White S. D. M., 1997, *ApJ*, 490, 493
- Neto A. F., Gao L., Bett P., Cole S., Navarro J. F., Frenk C. S., White S. D. M., Springel V., Jenkins A., 2007, *MNRAS*, 381, 1450
- Oguri M., Bayliss M. B., Dahle H., Sharon K., Gladders M. D., Natarajan P., Hennawi J. F., Koester B. P., 2012, *MNRAS*, 420, 3213
- Oguri M., Takada M., Umetsu K., Broadhurst T., 2005, *ApJ*, 632, 841
- Okabe N., Okura Y., Futamase T., 2010a, *ApJ*, 713, 291
- Okabe N., Takada M., Umetsu K., Futamase T., Smith G. P., 2010b, *PASJ*, 62, 811
- Perlmutter S., Aldering G., della Valle M., Deustua S., Ellis R. S., Fabbro S., Fruchter A., Goldhaber G., Groom D. E., et al. 1998, *Nature*, 391, 51
- Perlmutter S., Aldering G., Goldhaber G., Knop R. A., Nugent P., Castro P. G., Deustua S., Fabbro S., Goobar A., et al. 1999, *ApJ*, 517, 565
- Rasia E., Meneghetti M., Martino R., Borgani S., Bonafede A., Dolag K., Ettori S., Fabjan D., Giocoli C., Mazzotta P., Merten J., Radovich M., Tornatore L., 2012, *ArXiv e-prints*
- Rix H.-W., de Zeeuw P. T., Cretton N., van der Marel R. P., Carollo C. M., 1997, *ApJ*, 488, 702
- Sereno M., Zitrin A., 2012, *MNRAS*, 419, 3280
- Shaw L. D., Weller J., Ostriker J. P., Bode P., 2006, *ApJ*, 646, 815
- Sheth R. K., Mo H. J., Tormen G., 2001, *MNRAS*, 323, 1
- Sheth R. K., Tormen G., 1999, *MNRAS*, 308, 119
- Sheth R. K., Tormen G., 2004, *MNRAS*, 349, 1464
- Springel V., White S. D. M., Jenkins A., Frenk C. S., Yoshida N., Gao L., Navarro J., Thacker R., Croton D., Helly J., Peacock J. A., Cole S., Thomas P., Couchman H., Evrard A., Colberg J., Pearce F., 2005, *Nature*, 435, 629
- Springel V., White S. D. M., Tormen G., Kauffmann G., 2001b, *MNRAS*, 328, 726
- Tormen G., Diaferio A., Syer D., 1998, *MNRAS*, 299, 728
- Umetsu K., Birkinshaw M., Liu G.-C., Wu J.-H. P., Medezinski E., Broadhurst T., Lemze D., Zitrin A., Ho P. T. P., Huang C.-W. L., Koch P. M., Liao et al., 2009, *ApJ*, 694, 1643
- van den Bosch F. C., Tormen G., Giocoli C., 2005, *MNRAS*, 359, 1029
- Wang L., Li C., Kauffmann G., De Lucia G., 2006, *MNRAS*, 371, 537
- Wechsler R. H., Bullock J. S., Primack J. R., Kravtsov A. V., Dekel A., 2002, *ApJ*, 568, 52
- White S. D. M., Rees M. J., 1978, *MNRAS*, 183, 341
- Zhao D. H., Jing Y. P., Mo H. J., Bnörner G., 2009, *ApJ*,

707, 354

Zitrin A., Broadhurst T., Umetsu K., Coe D., Benítez N.,  
Ascaso B., Bradley L., Ford H., Jee J., Medezinski E.,  
Rephaeli Y., Zheng W., 2009, MNRAS, 396, 1985